AIAA JOURNAL
Vol. 47, No. 1, January 2009

Active Control of a High Reynolds Number Mach 0.9 Axisymmetric Jet

J.-H. Kim,* J. Kastner,† and M. Samimy‡
The Ohio State University, Columbus, Ohio 43235-7531

DOI: 10.2514/1.36801

Active control of a Mach 0.9 circular jet with a Reynolds number of 7.6×10^5 was conducted using eight localized arc filament plasma actuators, equally spaced azimuthally just upstream of the nozzle exit. Detailed two-component particle image velocimetry measurements were carried out on a streamwise plane passing through the jet centerline. The forcing Strouhal number was varied from 0.09 to 3.08 at azimuthal modes $m = 0$–3, ± 1, ± 2, and ± 4, the attainable modes with eight actuators. The spreading of the jet with downstream distance was used as a metric for determining the optimum forcing Strouhal number at a given azimuthal mode. For all azimuthal modes except $m = 3$, the most effective forcing was at a Strouhal number of about 0.3, which is in agreement with the results in the literature for low-Reynolds-number and low-speed flows. For a $m = 3$ mode, the maximum spreading was achieved at a forcing Strouhal number of 0.09. For a fixed Strouhal number at about 0.3, the flapping mode ($m = \pm 1$) resulted in best entrainment and mixing, or jet spreading. Conditionally sampled velocity contours were used to obtain Galilean velocity field and streamlines, which were used to reveal the evolution and interaction of the generated large-scale structures and their roles in the jet development and spreading. The nature of jet spreading and development are explained by the dynamics of large-scale structures, including the mutually and self-induced velocity field. The convection velocity of the generated large-scale structures was determined using the spatial correlation of the velocity field for various forcing Strouhal numbers and modes, which varied from approximately $0.55U_j$ to $0.75U_j$ for lower to higher forcing Strouhal numbers, respectively.

Nomenclature

D	=	nozzle exit diameter
f	=	frequency
m	=	azimuthal mode
St_D	=	Strouhal number based on the nozzle diameter D ($=fD/U_j$)
St_{DF}	=	forcing Strouhal number based on the nozzle diameter D
St_θ	=	Strouhal number based on the boundary-layer momentum thickness θ ($=f\theta/U_j$)
U_j	=	jet exit velocity
x	=	streamwise coordinate
y	=	vertical coordinate
z	=	spanwise coordinate
δ	=	calculated jet width at half-centerline velocity
θ	=	boundary-layer momentum thickness at the nozzle exit
σ_u	=	rms of x-direction velocity
σ_v	=	rms of y-direction velocity
σ_v/σ_u	=	anisotropy ratio
τ	=	duty cycle (=the percentage of on time in a forcing period)

Presented as Paper 0320 at the 45th AIAA Aerospace Sciences Meeting and Exhibit, Reno, NV, 8–11 January 2007; received 23 January 2008; revision received 24 May 2008; accepted for publication 9 September 2008.

*Research Associate, Gas Dynamics and Turbulence Laboratory, Department of Mechanical Engineering, 2300 West Case Road. AIAA Member.

†Graduate Research Associate, Gas Dynamics and Turbulence Laboratory, Department of Mechanical Engineering, 2300 West Case Road; currently Research Assistant Professor, University of Cincinnati. AIAA Member

‡Howard B. Winbigler Professor of Engineering, Gas Dynamics and Turbulence Laboratory, Department of Mechanical Engineering, 2300 West Case Road; samimy.1@osu.edu. AIAA Associate Fellow (Corresponding Author).

I. Introduction

MANY researchers have worked on jet flow control to enhance mixing and/or reduce noise. Most of the earlier active jet flow control has been done in low-speed and low-Reynolds-number flows. In such flows, acoustic drivers were successfully used because both the flow momentum and the flow characteristic frequency are relatively low. However, acoustic drivers do not have sufficient bandwidth and amplitude to control high-speed and high-Reynolds-number flows, because the characteristic flow frequency and flow momentum increase with the jet speed and Reynolds number.

There are two major instability modes in a jet that could be used for jet control. These modes are based on the two length scales in a free jet: one is the boundary-layer momentum thickness θ at the nozzle exit, and the other is the nozzle exit diameter D for a circular nozzle or nozzle exit height h for a rectangular nozzle. The initial shear layer instability frequency is scaled with the momentum thickness of the boundary layer at the nozzle exit. The jet column instability or the jet preferred mode is amplified further downstream near the end of the potential core, and its frequency is scaled with the nozzle exit diameter or height. The corresponding Strouhal numbers are St_θ ($=f\theta/U_j$) and St_D ($=fD/U_j$) for the initial shear layer instability and the jet column mode, respectively, where f and U_j are the instability wave or the large-scale structures passage frequency and the jet exit velocity, respectively.

In the initial shear layer, the maximum amplification of disturbances occurs around St_θ of 0.012 in unperturbed jets [1], whereas the maximum amplification rate of disturbances occurs around St_θ of 0.017 [2,3]. The input excitation amplitude required to control this instability in low-speed flows is very small, and linear instability analysis has been used extensively to explore various aspects of this instability [3]. When forcing around St_θ of 0.017, the increased amplification rate leads to earlier saturation of amplification and breakdown of vortices into smaller scales so that the amplification of the instability is smaller than that in unperturbed jets [1]. However, the growth of instability at $St_\theta = 0.012$ leads to the large-scale structures in the shear layer of the jet, which are responsible for the entrainment of ambient air into the jet and gross mixing with the jet fluid.

The maximum amplification of the jet column instability occurs over a wide range of St_D from 0.2 to 0.6 [4–7], heavily dependent

upon the experimental facility. This is presumably due to the variations of the naturally occurring disturbances in the experiments, as well the measurement location and technique. The jet column mode can be excited directly by forcing the jet with sufficiently high amplitude [4].

In high-Reynolds-number and high-speed flows, the actuator must have high-bandwidth and high-amplitude because the instability frequencies and flow momentum are also high. To meet this requirement, a plasma-based actuation system has been developed, which is called localized arc filament plasma actuators (LAFPAs). LAFPAs can provide excitation signals of high amplitude and high frequency for high-speed and high-Reynolds-number flow control [8–11]. The plasma actuators were effective in forcing the jet column mode of an ideally expanded Mach 1.3 jet [10]. Whereas the jet responded to actuation over a large range of St_D and at various azimuthal modes, the maximum spreading occurred around a St_D of 0.3. The duty cycle of the plasma actuator also played a significant role, and the best results were observed at a lower value of 5–10%.

The plasma actuators were also used in a Mach 0.9 jet, and the results showed that the jet noise was reduced when forcing Strouhal numbers around 1.1 and higher were used [9]. The level of noise reduction depended on both forcing frequency and azimuthal mode. The plasma actuators were also used, though on a limited capacity, due to the lack of proper power supply, in a larger nozzle with an exit diameter of 19.05 cm to test their scalability [12]. These tests showed that the effects of forcing in a larger jet were similar at a Mach number of 0.5. However, the actuator appeared to lack control authority at higher Mach numbers due to the limitation of the plasma generation system/power supply used, which was designed for a smaller-scale jet.

In the earlier Mach 0.9 jet work with the plasma actuators, limited flow results were obtained and two main open questions were as follows:

1) What kind of structures are generated by excitation of the jet with the actuators?

2) What is the role of generated structures in the jet development?

Thus, the purpose of the present research is to further explore the Mach 0.9 jet controlled by the plasma actuators at various azimuthal modes and frequencies, to identify large-scale structures in the jet plume, and to further the understanding of how the vortex dynamics are related to the jet development.

II. Facility and Techniques

All the experiments were conducted at the Gas Dynamics and Turbulence Laboratory at The Ohio State University. Compressed air was filtered, dried, and stored in two cylindrical tanks with a capacity of 43 m^3 and up to 16 MPa. The compressed air is supplied to the stagnation chamber of a 2.54-cm-axisymmetric nozzle. Then, the air is discharged through the converging nozzle. A boron nitride extension is attached to the converging nozzle to house eight plasma actuators. Each actuator is composed of a pair of 1-mm tungsten electrodes. All electrodes are placed approximately 1 mm upstream of the nozzle extension exit. There is a small groove in the boron nitride extension, measuring 1 mm wide and 0.5 mm deep, to house the electrodes and to avoid the plasma from being blown away by the flow. All experiments were conducted at a Mach number of 0.9, with a Reynolds number based on nozzle exit diameter of 7.6×10^5. The coordinate system is shown in Fig. 1: X, Y, and Z are, respectively, streamwise, vertical, and spanwise direction.

The plasma-generating system uses two high-voltage Glossman dc power supplies of 10 kV and 1 A maximum output each. Each power supply can drive four actuators, allowing operation of up to eight actuators at the same time. Each actuator is independently controlled by a Behlke high-voltage (HV) transistor switch, as depicted in Fig. 2. A National Instrument (NI) digital-to-analog converter (DAC) is used to generate eight independent pulse trains to control the transistor switches. The forcing frequency, duty cycle, and azimuthal mode are independently controlled through NI LabView software. The azimuthal modes used in the present research are $m = 0$–3, ± 1, ± 2, and ± 4, which are the only modes available

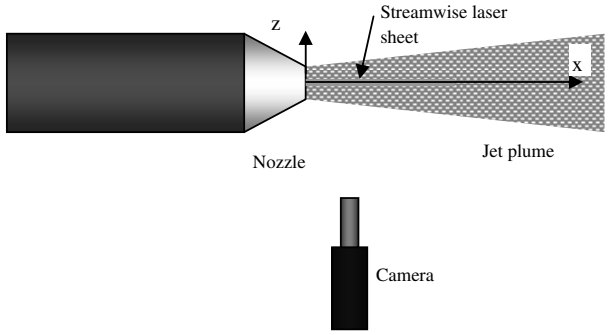

Fig. 1 Schematic of the jet and the PIV set up. *Y* coordinate is normal to the plane.

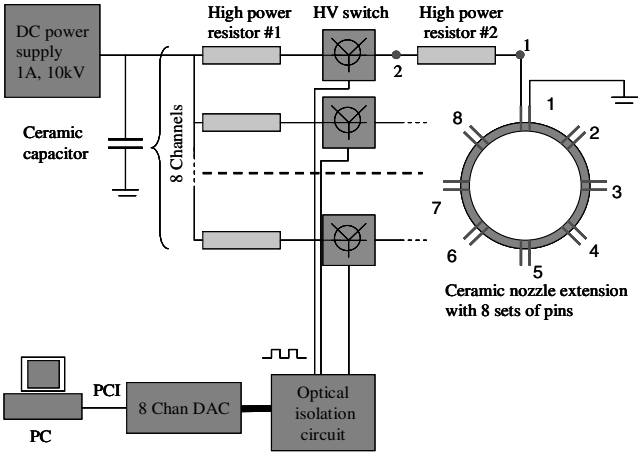

Fig. 2 Schematic of the in-house fabricated plasma generator.

when using eight actuators. A detailed description of the modes is given in Table 1, and a mathematical expression of azimuthal modes is given in [10]. Because the plasma actuator has either a "positive" or a zero input, the azimuthal modes are not determined the conventional way, as in a typical acoustic driver with a sinusoidal input. At each mode, the forcing Strouhal number St_{DF} was varied from 0.09 to 3.08, covering both the jet column mode and shear layer instability mode. The duty cycle τ (the percentage of on time relative to the period of the control signal) is set by one of two relationships:

$$\tau = 6.62St_{DF} + 2 \quad \text{for } St_{DF} < 1.81 \tag{1}$$

$$\tau = 1.15St_{DF} + 15.7 \quad \text{for } St_{DF} \geq 1.81 \tag{2}$$

These relations were determined experimentally to provide the maximum mixing/spreading at each forcing Strouhal number. A continuous pulse train is used to operate the actuators.

The thickness of the nozzle extension is $0.6D$ (15 mm). With this extension, the momentum and boundary-layer thickness at the extension exit is estimated to be about 0.1 and 1 mm, respectively [13]. One major parameter representing nozzle exit conditions is the ratio of nozzle exit diameter to the momentum thickness (D/θ). In the present research, the exit boundary layer is very thin since $D/\theta(\sim 250)$ is much larger than one.

The jet flow velocity (with an exit centerline velocity of 280 m/s) is measured by a LaVision particle image velocimetry (PIV) system, which has two cameras with 2048×2048 pixel resolution. A Spectra Physics Model SP-400 dual head Nd:YAG laser is used for the light source. The cameras and laser are synchronized by a timing unit housed in a dual processor PC. Only two components of velocity on a streamwise plane are measured by one camera, as depicted in Fig. 1. The spatial resolution of the velocity vectors depends on the field of view and the number of pixels used. For most of the streamwise velocity field measurements, the spatial resolution is

Table 1 Descriptions of forced azimuthal modes

Mode	Description	Remarks
$m = 0$	All actuators are operated at the same time	
$m = 1$–3	The phase delay between each neighboring actuator is $m(360/8)$ deg	The phase delay between actuators 1 and 2 is 45, 90, and 135 deg for $m = 1$, 2, and 3, respectively.
$m = \pm 1$	The top three actuators (1, 2, and 8) are operated at the same time. The bottom three actuators (4–6) are operated at the same time, but 180 deg out of phase with the top three.	The node points are at actuators 3 and 7.
$m = \pm 2$	Any two consecutive actuators are grouped together (1–2, 3–4, 5–6, 7–8) and the first and third groups are operating in phase; the second and fourth group are operating in phase, but 180 deg out of phase with the other two.	There is a nodal point between each neighboring group (e.g., between actuators 2 and 3).
$m = \pm 4$	All odd number actuators are grouped together and operating in phase, but 180 deg out of phase with the even-number actuators, which are grouped together.	There is a nodal point between any two consecutive actuators (a total of eight nodal points).

about 1.9 mm. The laser sheet thickness is less than 0.3 mm. The time separation between two consecutive PIV images was 1.8 μs, and so the velocity field from a pair of PIV images is almost instantaneous. Initially, an interrogation window of 64×64 pixels was used. Then, the reduced data with a 64×64 pixel window was used as a reference in final processing, with an interrogation window of 32×32 pixels. Each consecutive interrogation window was overlapped by 50% to increase spatial resolution.

The jet plume is seeded with DEHS (diethylhexyl-sebecat) liquid droplets by a four-jet LaVision atomizer. A 38.1-cm duct, made of 1-mm-thick sheet metal, is placed around the jet and extending upstream of the jet exit to generate a very low-speed coflow. The exit plane of the duct is at 2.5 cm upstream of the nozzle exit to avoid blocking the laser sheet during PIV measurements. The coflow is generated without using any fans or blowers by simply allowing a significant portion of the entrained ambient air into the jet to pass through the duct. The coflow is seeded by a Concept Model ViCount Compact 1300 fogger to avoid spurious velocity vectors in the entrained air that has not yet mixed with the jet. The ViCount smoke generator is good for any applications with higher seeding rate and without backpressure. On the other hand, the LaVision atomizer is good for any application with relatively low seeding rates with some backpressure (up to 10 bar). The average droplet size is about 0.7 and 0.25 μm for the jet flow and coflow, respectively. It is assumed that the jet flow is not affected significantly by the coflow with a velocity of less than 3 m/s (about 1% of the jet exit velocity). The turbulence statistics were converged when 600–650 image pairs were used. Thus, about 700 image pairs were used for all the statistics reported in this paper.

The uncertainty in the PIV measurements is related to many parameters, such as the particle size and density and turbulence frequency of interest. With 5% deviation from actual turbulence intensity, the seeded particles trace the flow up to 20 and 70 kHz of turbulence frequency for 0.3 and 0.7 μm particles, respectively [14]. According to this calculation, the uncertainty of turbulence intensity is about 5% up to Strouhal number of 1.8. However, the uncertainty level for the mean and turbulence quantity was within ± 3 and ± 15%, respectively, based on the repeatability measurements for the baseline (BL) jet.

III. Results and Discussions

Detailed two-component PIV measurements on a streamwise plane passing through the jet centerline are used to explore the effects of forcing Strouhal number and azimuthal mode on the Mach 0.9 jet. The overall performance of the plasma actuators at each Strouhal number and mode will be discussed by using the average velocity images and turbulence statistics. Then, conditionally averaged velocity components superimposed on conditionally averaged streamlines will be used to investigate the dynamics of vortices or large-scale structures and their roles in the jet development.

A. Effects of Forcing Strouhal Number on Overall Jet Spreading

The jet was forced at forcing Strouhal numbers St_{DF} ranging from 0.09 to 3.08 for all available azimuthal modes. However, only results for $m = 0$, 1, 3, and ± 1 modes will be presented in this section. The centerline velocity decay has been widely used as a measure of the jet spreading or mixing with the ambient air, as it is often the only available result. The centerline velocity decay increases as the jet spread increases, in most cases. In the present research, growth of the full width at half-maximum (FWHM) streamwise velocity (jet centerline velocity) will be used, instead of the centerline velocity decay, as a measure for the jet spreading or mixing. Because the centerline velocity decay is an indirect measure, it could be misleading in some cases where the jet cross section is not circular.

For $m = 0$ mode, the jet width (calculated by using FWHM and referred to as the jet width henceforth) is shown in Fig. 3, along with the jet centerline Mach number and the measured two-component turbulence kinetic energy (TKE) profiles. The trend of jet width with the St_{DF} does not match the centerline Mach number decay trend at this mode. However, the trend of the centerline Mach number decay is quite similar to that of the centerline TKE development. As will be shown later, the mismatch of these trends is observed only at the axisymmetric mode ($m = 0$). At this point, it is not clear why they are so different at this mode.

The jet width shows the effects of forcing on the jet spreading for the entire streamwise measurement extent, whereas the centerline Mach number decay provides the overall mixing/spreading effect only beyond the potential core. When the jet was forced at a Strouhal

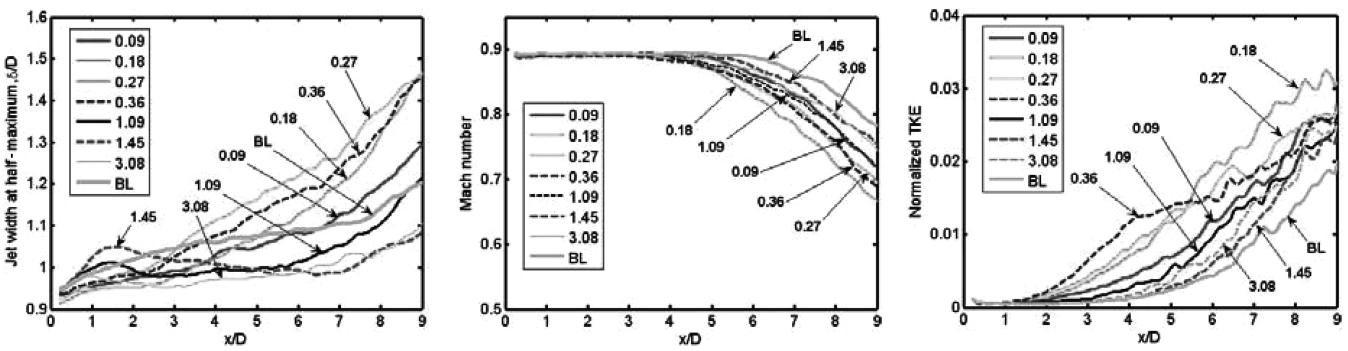

a) Jet width (FWHM) b) Centerline mach number c) Centerline TKE

Fig. 3 Jet width development with a) downstream locations, b) centerline Mach number decay, and c) centerline TKE at $m = 0$.

number near or below 0.36, the jet width grew almost linearly in the downstream direction for the entire measured x/D. The best spreading/mixing was observed at $St_{DF} = 0.27$, where the jet width was increased by about 20% at $x/D = 9$. The jet width grew faster and saturated closer to the nozzle exit when the jet was forced at higher Strouhal numbers, resulting in significant mixing reduction by $x/D = 9$.

As the forcing Strouhal number is increased, the saturation occurred earlier because the generated structures are smaller and thus their life span is shorter. At a St_{DF} equal or greater than 1.0, the jet width was reduced upstream of $x/D = 2$ and remained unchanged up to $x/D = 6$ (which approximately marks the end of the potential core). The jet spreading was reduced by forcing at a higher St_D, most likely by suppressing the formation and/or development of large-scale structures, which play an important role in entrainment and jet spreading/mixing. The far-field acoustic results showed that the broadband noise level was reduced when the jet was forced at high forcing Strouhal numbers [9]. The jet width variation is consistent with the far-field noise results at the same conditions.

Figure 4 shows the development of jet width and the centerline Mach number at the $m = 1$ mode. For this mode, unlike for the $m = 0$ mode, the trend of the centerline Mach number is similar to that of the jet width development downstream of x/D of about five. Although not shown, the trend of the centerline TKE matches with these two trends as well. As mentioned earlier, the three trends are very similar for all the azimuthal modes tested, except for $m = 0$.

For $m = 1$, the growth of the jet width was maximum when forcing at $St_{DF} = 0.18$, and only a slightly lower growth was observed at $St_{DF} = 0.27$ and 0.32. For these three forcing cases, as well as others with relatively strong jet spreading, the initial linear growth of the jet width was stopped near the end of potential core before starting another linear growth region, but with much larger slope. At St_{DF} of 0.36 (not shown here) and higher, there was a region of almost zero growth rate, as clearly observed at a St_{DF} of 1.09. The significantly reduced growth near the end of the jet potential core is due to the cross-centerline interaction of large-scale structures in this region. This will be further discussed in Sec. III.D.

For $m = 1$ mode, the initial growth rate of the jet width was increased over that of the baseline at St_{DF} numbers greater than 1.0, but decreased for St_{DF} numbers less than 0.7. The saturation in the jet width growth occurred earlier, and the saturated jet width also decreased as the St_{DF} increased, which is similar to what was found at $m = 0$ mode. In the near field, the growth and saturation of the jet width with the St_{DF} is consistent with the pressure perturbation level measurements along the nozzle lip line using a single actuator [9]. The jet width remained about the same after it saturated, and the jet growth was suppressed at high St_{DF} numbers, as was true for the $m = 0$ mode. As will be discussed in a later section, the quick jet width saturation with increasing St_{DF} is due to the smaller structures and their shorter life span when forcing the jet at higher frequencies.

Figure 5 shows the growth of the jet width when the jet was forced at $m = 3$ mode. This azimuthal mode had significant noise reduction over a wide range of St_{DF} numbers [9]. The initial growth of the jet width was significantly increased compared with the lower azimuthal

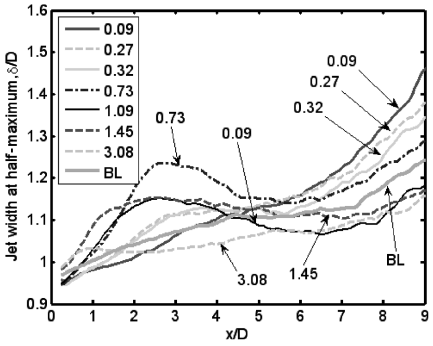

Fig. 5 Jet width growth for $m = 3$ mode.

modes, especially at $St_{DF} = 0.73$. At this St_{DF}, the jet width experienced decay near the end of the potential core, followed by a modest growth rate. For St_{DF} numbers greater than one, the jet width became narrower than the baseline width at far downstream locations, although it was wider at near-field locations. As was seen at other St_{DF} numbers, the jet width developed almost monotonically when forced at low St_{DF} numbers. The maximum jet spreading was found at the lowest St_{DF} of 0.09.

For the first combined mode ($m = \pm 1$), often referred to as the flapping mode, the jet width growth on the flapping plane is shown in Fig. 6a. The trend of the jet width growth is consistent with the centerline Mach number decay, as shown in Fig. 6b. Note that the ordinate scale in Fig. 6a is over twice that for the other modes presented earlier. In the upstream region, the trend of the jet width growth with St_{DF} is similar to that for the $m = 1$ mode. Similar to the results for the other modes presented, the growth in jet width is suppressed when the jet is forced at higher St_{DF} numbers, as can be seen at 3.08. The jet width was increased significantly near $St_{DF} = 0.3$, and the maximum growth was at $St_{DF} = 0.27$, approximately 3 times that of the baseline at $x/D = 9$. At low St_{DF} numbers, the jet width grows monotonically up to $x/D = 4$, which is near the end of the potential core. When St_{DF} is increased or decreased from 0.27, the jet spreading is decreased very rapidly. At St_{DF} of 0.09 and 0.73, the jet width increased monotonically (almost linearly) with downstream location. The growth in jet width near $St_{DF} = 0.3$ started to increase exponentially at $x/D = 4$, where the potential core ends, as seen in Fig. 6b. As with the other azimuthal modes, the enhanced growth resulted in a reduction in the jet potential core. The potential core length was reduced to $x/D = 4$ for the best mixing case from $x/D = 6$ for the baseline case (Fig. 6b).

As was presented and will be further discussed later, the most effective forcing was at $m = \pm 1$ mode, as far as the jet spreading is concerned. For this mode, the average streamwise velocity contours are shown in Fig. 7 at $St_{DF} = 0.18$, 0.27, 0.72, 1.08, and 3.08. The results in Fig. 7 are on the flapping plane of the jet. The jet exit velocity is about 280 m/s and varies slightly, depending on the jet stagnation temperature. In the figure, the black background is for the coflow where the velocity is less than 3 m/s (about 1% of the jet exit

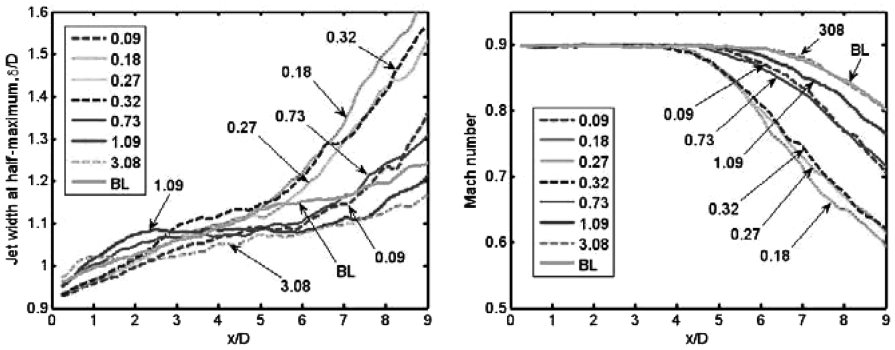

a) Jet width **b) Centerline mach number**

Fig. 4 Growth of the jet width with a) downstream locations and b) centerline Mach number decay at $m = 1$.

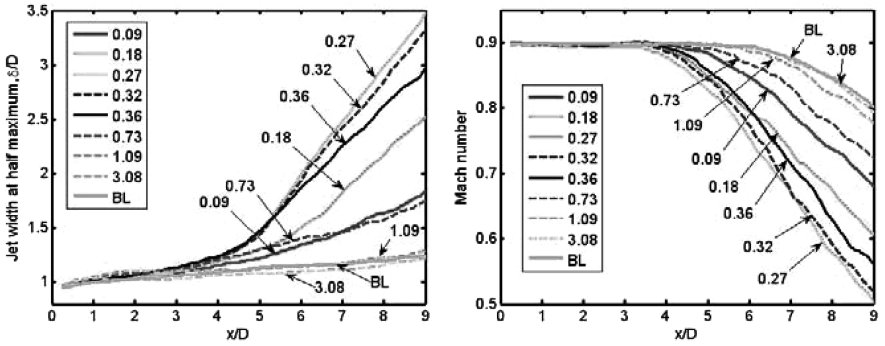

a) Jet width b) Centerline mach number

Fig. 6 Development of a) jet width and b) centerline Mach number for $m = \pm 1$ mode on the flapping plane. Note that the ordinate scale in Fig. 6a is over twice the others in Figs. 3–5.

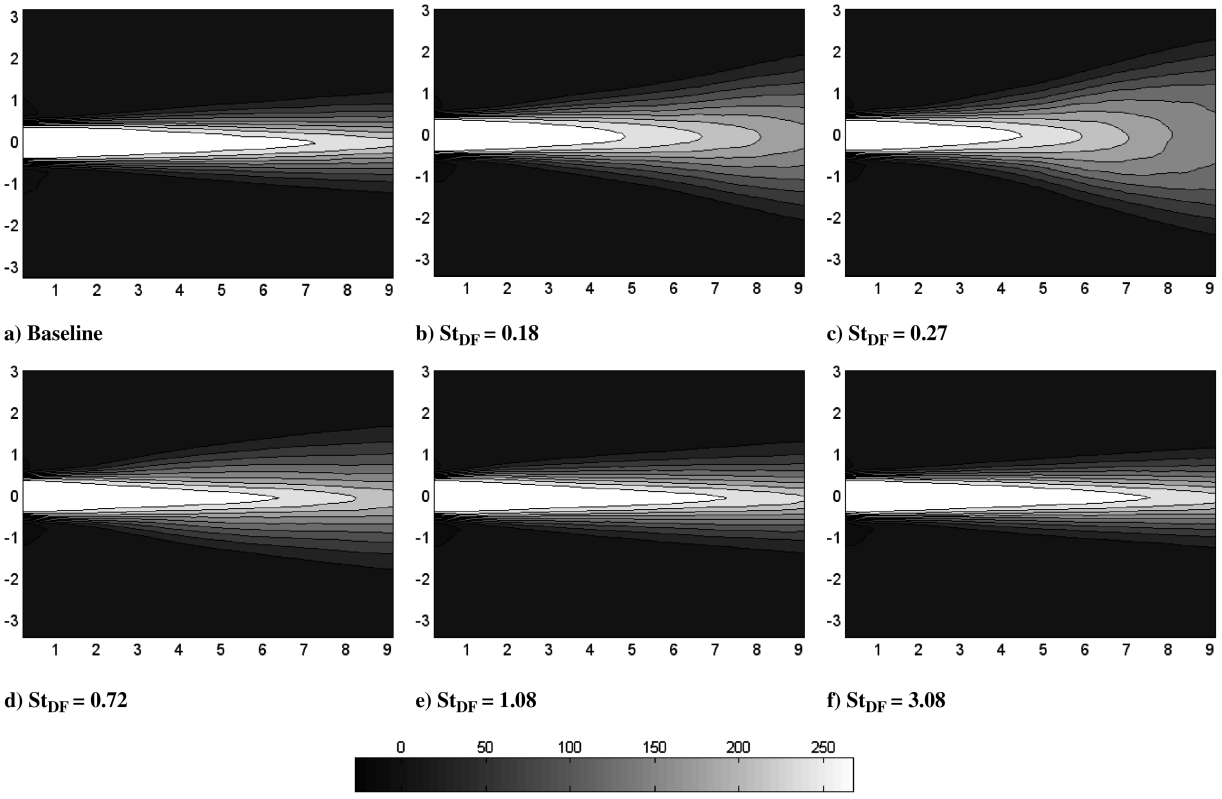

a) Baseline b) $St_{DF} = 0.18$ c) $St_{DF} = 0.27$

d) $St_{DF} = 0.72$ e) $St_{DF} = 1.08$ f) $St_{DF} = 3.08$

Fig. 7 Average streamwise velocity field for various forcing Strouhal numbers at $m = \pm 1$. The velocity scale is in meters per second and the exit jet velocity is about 280 m/s.

velocity) and is not expected to affect the jet development significantly.

As St_{DF} increases, the jet spreading angle increases until it reaches a maximum around $St_{DF} = 0.3$, beyond which it decreases slowly. The jet spreading is almost the same as that of the baseline jet when forcing at St_{DF} numbers greater than about 1.0. The results suggest that forcing around a St_{DF} of 0.3 is the most effective in spreading the jet, which is the jet preferred St_{DF} at this mode. The jet preferred Strouhal number, reported in the literature for the past 10–20 years, varies from 0.2 to 0.6. The same plasma actuators were also used to force an ideally expanded Mach 1.3 jet, and flow visualization results were used to conclude that the jet column mode was around 0.3 [10].

When the jet was forced at about $St_{DF} = 0.3$, the jet potential core length was significantly shortened, as shown in Fig. 7c. This can be more readily seen in Fig. 6b, which shows the centerline Mach number distributions with various forcing Strouhal numbers. The centerline Mach number decays the fastest at $St_{DF} = 0.27$. This is consistent with the highest jet spreading, shown in Fig. 7c. As the St_{DF} increases beyond about 0.3, the potential core increases, and becomes almost the same as that of the baseline jet for St_{DF} numbers greater than about 1.0.

The jet response to the forcing with plasma actuators was dependent on the forcing frequency, duty cycle, and azimuthal mode. The optimum forcing Strouhal number, where the jet spreading is maximum, depended on the forcing azimuthal mode as can be inferred from the results presented so far. Table 2 shows the optimal forcing Strouhal number for each mode based on the jet width in the region downstream of the jet potential core. The optimum St_{DF} is about 0.3 except for azimuthal modes 1 and 3. However, the Strouhal number for the second best is 0.27 for $m = 1$ mode, and the jet width growth at this value is very close to the optimum value. The only exception is $m = 3$ mode, which has a maximum jet width growth at $St_{DF} = 0.09$ (one-third of other cases).

B. Effects of Azimuthal Mode

As was presented earlier, the jet preferred Strouhal number, where the jet spreading/mixing is maximized, varied slightly for different

Table 2 Optimum forcing Strouhal number for each mode based on the jet width downstream of jet potential core region

Mode	0	1	2	3	±1	±2	±4
St_{DF}	0.27	0.18	0.36	0.09	0.27	0.32	0.32

azimuthal modes, but remained close to 0.3 for most modes except for $m = 3$, which was 0.09. The average streamwise velocity contours are shown in Fig. 8 for $m = 0$–3, ±1, ±2, and ±4 modes at St_{DF} corresponding to those in Table 2. For all modes, the jet spreading was significantly enhanced compared with that of the baseline jet (Fig. 7a), with the largest enhancement at $m = \pm1$ mode. A shorter visual potential core length is observed for greater jet spreading. This is more readily observed in the centerline Mach number profiles shown in Fig. 9a. The length of the potential core for $m = 1$ and ±2 modes is reduced by a similar amount. The least spreading was observed when exciting $m = \pm4$. As was discussed earlier, the mean velocity contours and the centerline Mach number only show the effects of forcing on the potential core length and the overall spreading downstream of the potential core.

The jet width development is shown in Figs. 9b and 9c, which show the effects of forcing over the entire region of the jet flow from the nozzle exit to $x/D = 9$. Figure 9b shows the jet width calculated from Fig. 8, and thus only shows the jet width on the PIV plane in this figure. Because the jet cross section at a far downstream location is near axisymmetric, Fig. 9b is appropriate for evaluating the overall spreading except for $m = \pm1$ mode. For $m = \pm1$ mode, the jet spreads significantly more in the flapping plane compared with the nonflapping plane. The cross section is assumed to be approximately elliptic, and thus the equivalent jet width for $m = \pm1$ was calculated from the square root of the multiplication of jet widths on the flapping and nonflapping planes, to take into account the highly nonaxisymmetric spreading. The results for all the modes are shown in Fig. 9c. The trend of equivalent jet width is consistent with the centerline Mach number except for $m = 0$ mode. This is due to the relatively slow decay of the centerline Mach number for $m = 0$ mode, as will be discussed later. Although the centerline Mach number showed some disparity, it can still be used as a measure of the overall jet spreading. This is the reason many researchers have used the centerline velocity decay as an indicator of the jet spreading.

The equivalent jet width also shows that the maximum and minimum jet spreading was obtained at $m = \pm1$ and $m = \pm4$ modes, respectively. For $m = 2$, ±1, and ±4 modes, the jet width grew significantly over the other modes in the initial region or near field. However, the growth rate of the jet width for $m = 2$ and ±4 decreased near the end of the potential core, and thus this led to a limited increase in jet widths by $x/D = 9$. For $m = \pm2$ mode, the jet width saturated from $x/D = 2.5$ until $x/D = 5$ (approximate end of the potential core), and then experienced rapid growth further downstream. At higher azimuthal modes of $m = 3$ and ±4, the jet centerline Mach number decay is slower and the increase in the jet width at a far downstream location is less than those of other modes. For $m = \pm2$, the centerline Mach number decay is comparable to that of $m = \pm1$, although the streamwise velocity contour is not comparable. In addition to the jet spreading, it seems that the vortex–

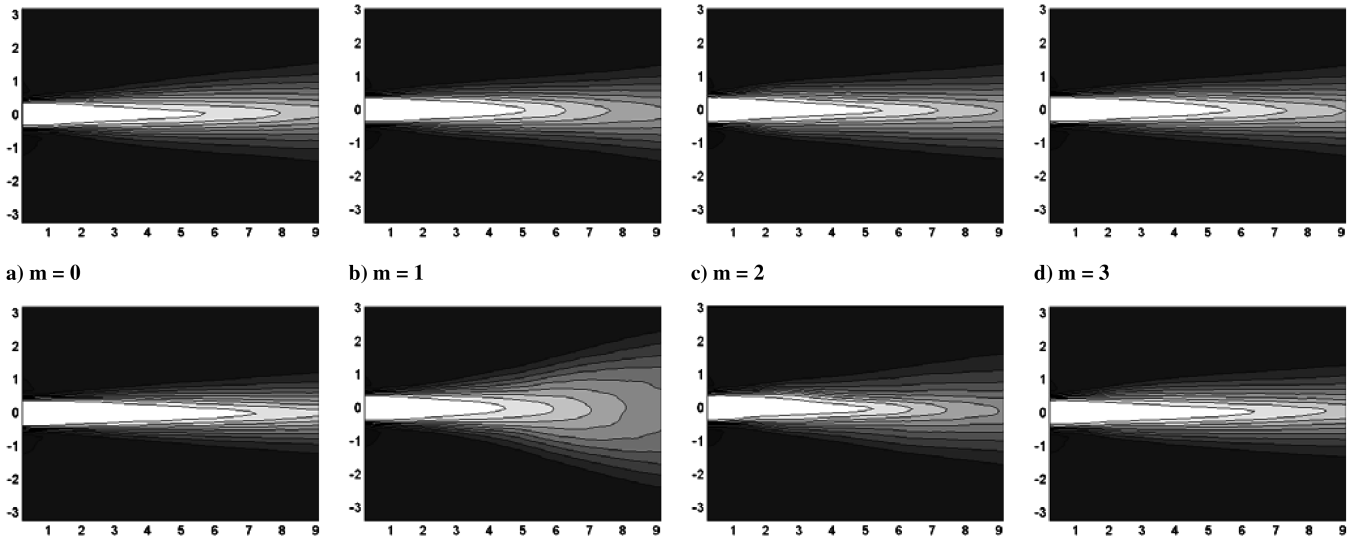

a) m = 0 b) m = 1 c) m = 2 d) m = 3

e) Baseline f) m = ±1 g) m = ±2 h) m = ±4

Fig. 8 Average streamwise velocity contours for various azimuthal modes at the St_{DF} numbers shown in Table 2.

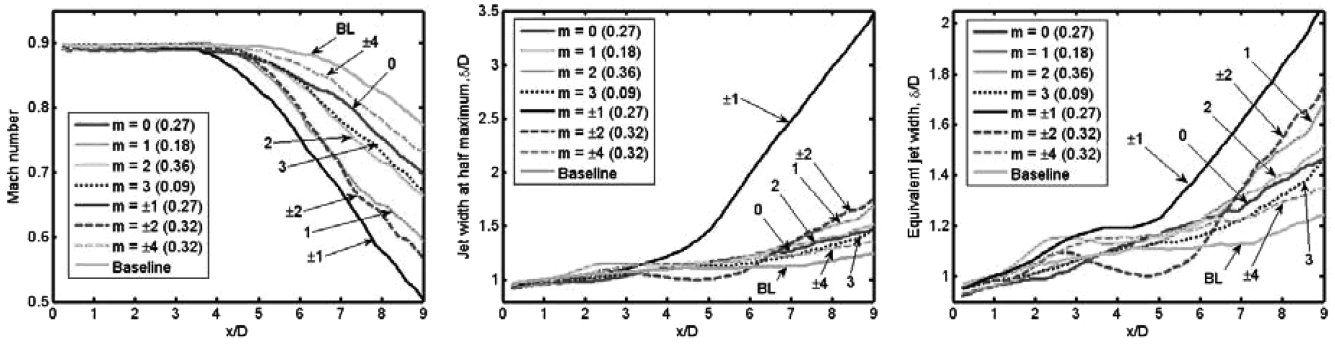

a) Centerline mach number b) Jet width c) Equivalent jet width

Fig. 9 Development of centerline Mach number and jet width at various azimuthal modes at St_{DF} numbers shown in Table 2.

vortex interaction across the jet column is another factor related to the centerline Mach number decay. This will be further discussed later by using large-scale structures and their dynamic interaction.

C. Effects Forcing on Turbulence Statistics

As presented in the previous section, changes in the mean flow characteristics depend significantly on the St_{DF} and forcing azimuthal mode. In this section, the effects of forcing on the turbulence statistics will be explored along the jet centerline. The normalized two-dimensional turbulent kinetic energy and anisotropy ratio (σ_v/σ_u) along the jet centerline are shown in Fig. 10 for $m = 0$, 1, and 3 modes. For $m = 0$ mode, the TKE is increased for all St_{DF} numbers, with the maximum amplification occurring at $St_{DF} = 0.18$, which corresponds to the case where the centerline Mach number decayed the fastest (Fig. 3b). The TKE is more amplified at $St_{DF} = 0.32$ and 0.36 (not shown here) up to around the end of the potential core ($x/D \approx 5$). Up to $x/D = 1$–1.5, the anisotropic ratio is one, as expected, as the fluctuations are due to random noise and measurement errors. However, further downstream, the ratio is substantially less than one for forcing at $St_{DF} \leq 0.73$ and substantially larger than one for the baseline jet and for forcing at $St_{DF} \geq 1.09$ for the $m = 0$ case (Fig. 10d). At lower St_{DF} numbers, the streamwise (or x component) turbulence intensity was amplified more than the cross-stream (y component) turbulence intensity. At higher St_{DF} numbers, the scales of the generated structures are so small that their influence on the centerline is expected to be very limited, and thus the forcing effects are expected to be negligible. On the other hand, the scales of the induced structures are much larger at lower St_{DF} numbers, increasing interactions across the jet centerline and thus significantly altering the anisotropy ratio. The anisotropy ratio was reduced for all cases downstream of the potential core.

For $m = 1$, a significant amplification in TKE was observed over a wide range of St_{DF} numbers from 0.18 to 0.36 (not shown here). The growth in TKE is saturated around $x/D = 7$ for these forcing Strouhal numbers. Contrary to the $m = 0$ case, the anisotropy in Fig. 10e implies that the cross-stream velocity fluctuations are dominant over the streamwise velocity fluctuations for $St_{DF} = 0.18$–0.36 (0.36 case is not shown) in the potential core region. As will be discussed later, the difference is associated with the symmetric or asymmetric nature of the large-scale structures across the jet diameter. The turbulence field becomes more isotropic downstream of the potential core. Figure 10e shows that the anisotropy is saturated near the end of potential core. As the St_{DF} is increased, the amplification level decreases and the anisotropy is about the same level as the baseline jet case for St_{DF} numbers equal or greater than 1.8 (not shown here).

For $m = 3$, the amplification in TKE is moderate except for $St_{DF} = 0.09$ and 0.18, where the jet spreading was maximum. At a low St_{DF}, the anisotropy increased near the end of the potential core similar to that for $m = 1$, but the increase is moderate. Interestingly, the TKE level was reduced when the jet was forced at a St_{DF} greater than 1.0. The reduction in TKE at high St_{DF} numbers is related to the broadband noise suppression seen for this mode [9,15].

The development of TKE and anisotropy along the jet centerline for $m = \pm 1$ are shown in Fig. 11. A dramatic increase in TKE was observed at low St_{DF} numbers. The anisotropy also increased significantly at low St_{DF} numbers, but the trend showed some disparity from that of TKE. The increase in anisotropy means that the velocity fluctuations in the cross-stream direction are dominant over those in the streamwise direction, as was also seen for $m = 1$. Because the flapping plane is in the y direction, the domination of the cross-stream velocity fluctuations is expected. As the St_{DF} is increased, the development of TKE and isotropy approach the levels of the baseline jet.

Figure 12 shows the development of TKE and anisotropy at the modes and St_{DF} numbers, where the jet width was maximized as shown in Table 2. The interaction between the generated structures across the jet centerline is expected to be noticeable when the scale of structures is large and comparable to the jet diameter. The onset location, where the TKE starts to increase over the background level, appears to be approximately the same for all azimuthal modes, but the amplification rates are significantly different for each mode. For $m = 0$, the TKE developed monotonically with downstream location, and did not show any saturation in the measured range. At this mode, vortex rings were generated by the plasma actuators, as will be shown later, and the scale/size of the rings grew monotonically with downstream location, and thus the TKE was also

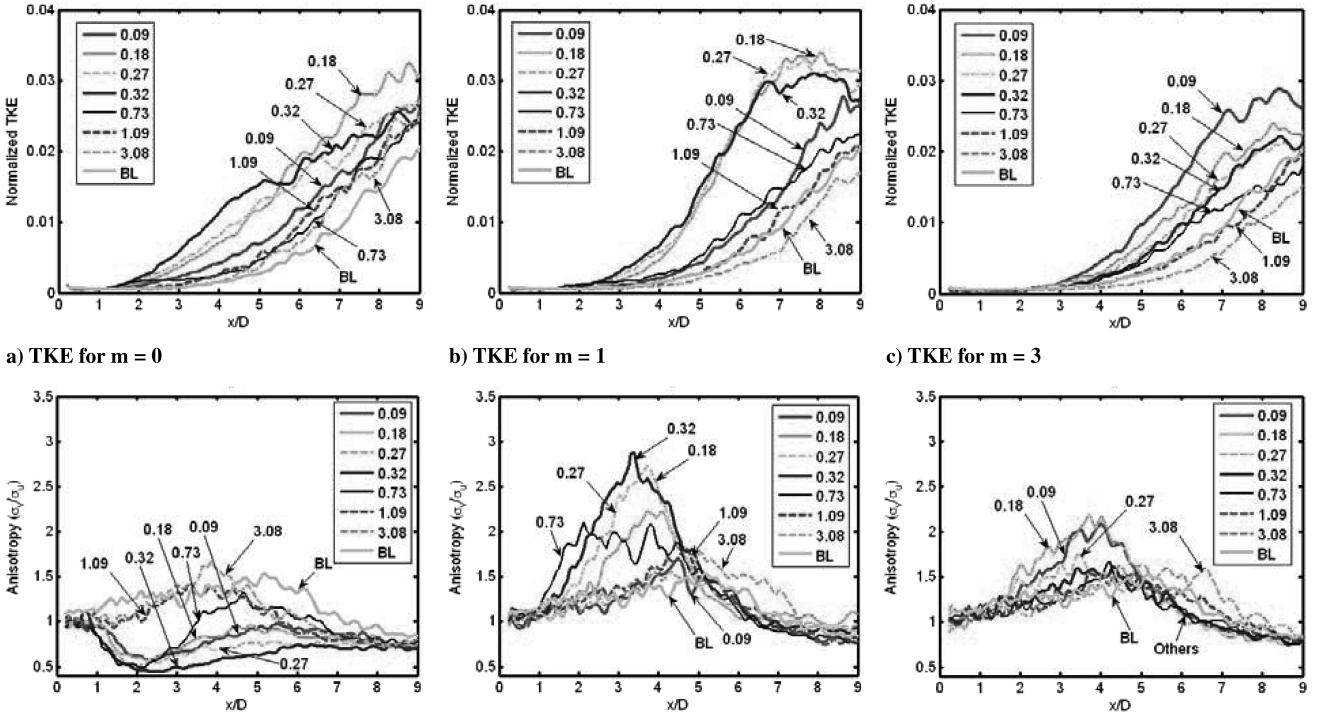

a) TKE for m = 0 b) TKE for m = 1 c) TKE for m = 3

d) Anisotropy for m = 0 e) Anisotropy for m = 1 f) Anisotropy for m = 3

Fig. 10 TKE and anisotropy for $m = 0$, 1, and 3 modes along the jet centerline.

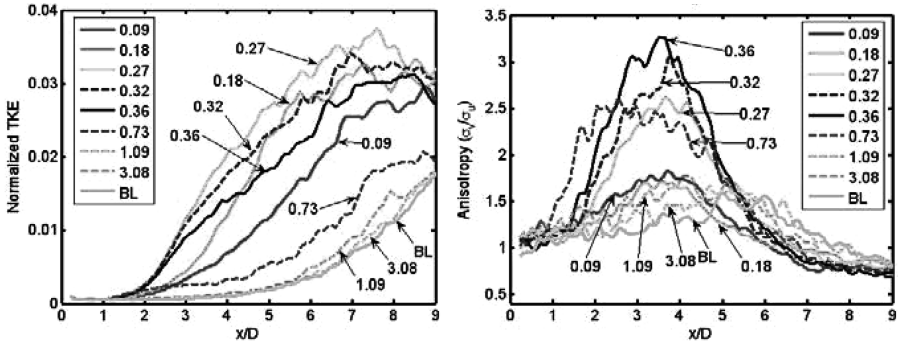

a) TKE b) Anisotropy

Fig. 11 TKE and anisotropy for $m = \pm 1$ mode along the jet centerline.

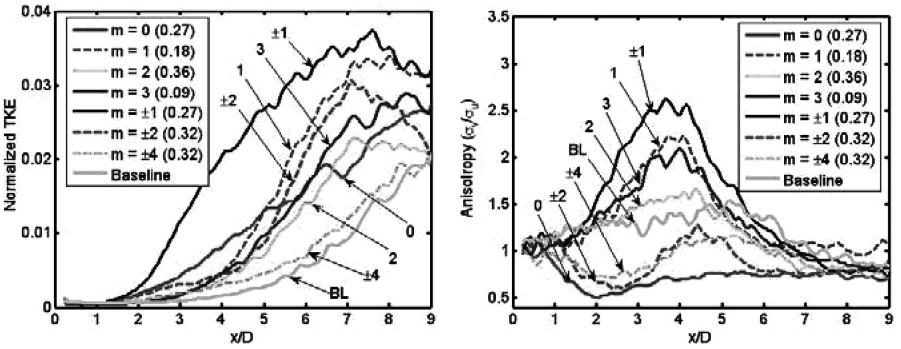

a) TKE b) Anisotropy

Fig. 12 Development of TKE and anisotropy at the St_{DF} numbers in Table 2.

expected to grow in such a fashion. For $m = \pm 1$, the TKE started to grow significantly as early as $x/D = 2$ and saturated around $x/D = 7$. The least amplification in TKE is observed for $m = \pm 4$ mode, where its growth rate is about the same as the baseline jet. For most cases, the growth in TKE is saturated around $x/D = 7$–8.

The development of anisotropy in Fig. 12b is very interesting. For even-numbered modes, anisotropy is decreased, implying the streamwise velocity fluctuations are dominant in TKE. The case for $m = 2$ seemed different, but the development at a lower St_{DF} is similar to other even-numbered modes. When the jet was forced at odd-numbered modes, the anisotropy is increased and saturated around $x/D = 3.5$. The anisotropy reached a minimum for the even-numbered modes around $x/D = 2$–2.5. These differences can be explained through vortex dynamics of the generated structures, as will be presented and discussed in the following section.

D. Vortex Dynamics and Its Role in the Jet Development

The overall effects of St_{DF} and forcing azimuthal mode were investigated and discussed in the earlier sections by using the average velocity contours, the jet width, TKE, and anisotropy. The average velocity and turbulence statistics are useful in evaluating the overall effects of St_{DF} and forcing azimuthal mode. However, they do not reveal details of flow structures and their role in the jet development. Thus, large-scale structures are extracted from PIV data and their dynamics are discussed in this section.

The Galilean decomposition is applied to the measured velocity fields to extract large-scale structures. The convection velocity of large-scale structures must be known to obtain the Galilean-decomposed velocity field. Once the convection velocity of large-scale structures is known, the Galilean-decomposed velocity field is obtained by subtracting the convection velocity from the measured velocity field [16]. Thus, in the Galilean decomposition, the reference frame moves at the convection velocity. A large-scale structure does exist and is visualized in the Galilean-decomposed velocity field if the streamlines make a closed loop or have a spiral pattern [17,18].

In the present research, a conditionally averaged velocity field was obtained and used for large-scale structures visualization. To get a conditionally averaged field from 700 instantaneous velocity fields, two-dimensional cross correlation was used to extract large-scale structures. A correlation window was taken in a given instantaneous velocity field. The velocity pattern within the window was correlated to the available 700 instantaneous velocity fields. All instantaneous images with a correlation level greater than a threshold value were ensemble averaged to form a conditionally averaged image of the 2-D velocity field. This is similar to the technique used in [19]. One could also use proper orthogonal decomposition for this purpose [20]. The next step is to calculate convection velocity of large-scale structures. Two-dimensional spatial correlations were used to calculate the spacing or wavelength of large-scale structures for the forced cases. The convection velocity is obtained by multiplying the large-scale structure spacing by the forcing frequency, as was done by Troutt and McLaughlin [21]. The last step to obtain a conditionally averaged Galilean-decomposed velocity field is to subtract the convection velocity from the conditionally averaged velocity field. Then, the large-scale structures are visualized when the Galilean streamlines are added, as was detailed in [17,18], and is shown in Fig. 13 for $m = \pm 1$ at St_{DF} numbers of 0.32, 0.72, and 1.08.

In the figure, the conditionally averaged Galilean streamlines and streamwise velocity magnitude (Fig. 13a) and cross-stream velocity magnitude (Fig. 13b) are superimposed. For the streamwise velocity, the dark and bright regions represent the slower and faster velocities, respectively. The maximum and minimum velocities are about 280 (in the potential core) and 3 m/s (in the ambient region). For the cross-stream velocity, the medium tone background represents near-zero velocity, and the brighter and darker tones indicate positive and negative velocities, respectively. In Figs. 13–15, the background velocity contours are added for ease of visualization. The figure shows the size and spacing of vortices, and the interaction between

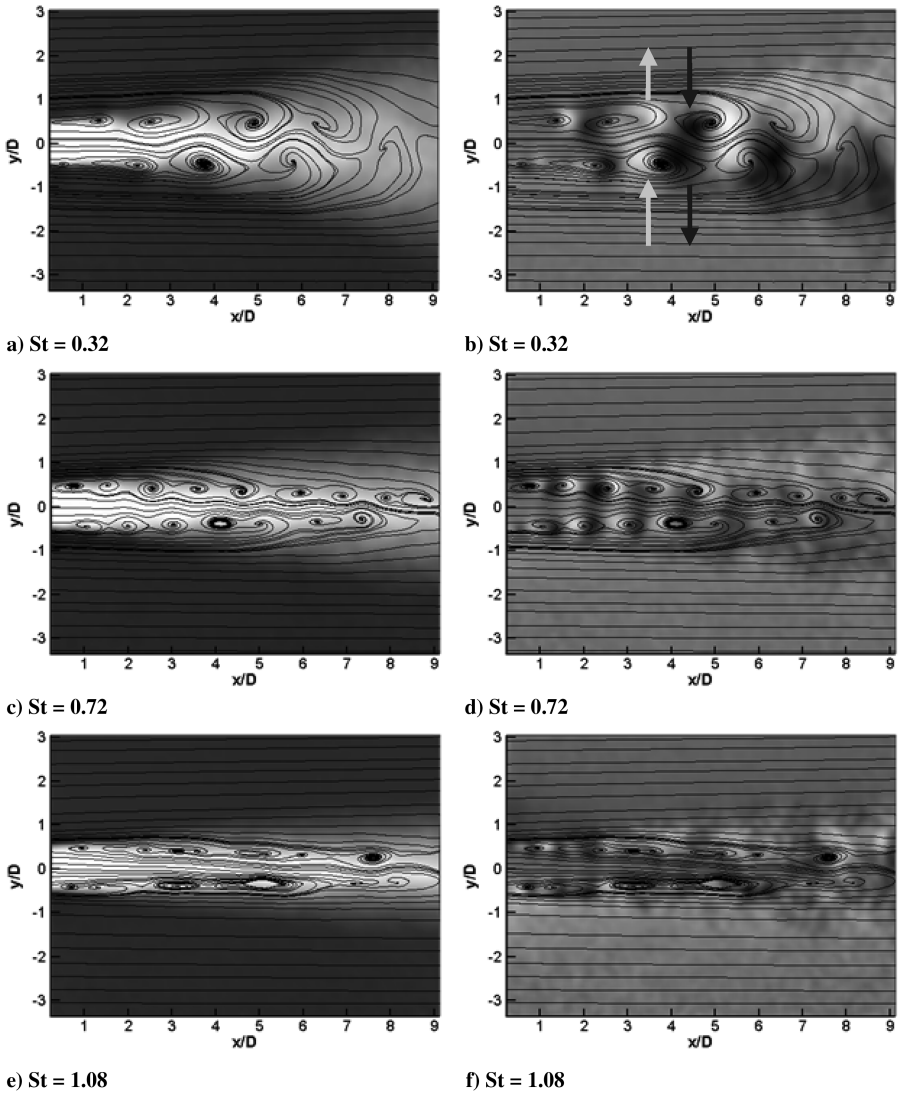

Fig. 13 Conditionally averaged Galilean-decomposed velocity fields and streamlines of streamwise (left column) and cross-streamwise (right column) velocities at $m = \pm 1$.

not only the vortices but also the vortices and the jet column. The large-scale structures generated by the forcing are robust and seem to be two-dimensional on the visualization plane, rotating either clockwise or counterclockwise, for those in the bottom shear layer and top shear layer, respectively.

At lower St_{DF} numbers, the generated large-scale structures are very well organized and their scale by the end of the potential core is comparable to the nozzle exit diameter. The vortices in the top and bottom shear layer are out of phase because the jet was forced with the first flapping mode ($m = \pm 1$). Downward velocity is induced in the downstream side of a vortex in the bottom shear layer and the upstream side of a vortex in the top shear layer, while upward velocity is induced in the upstream side of a vortex in the bottom shear layer and the downstream side of a vortex in the top shear layer, as indicated by arrows in Fig. 13b. The cross-stream velocity, induced by the vortices, appears strong enough to cause undulations in the jet column, which can be inferred from wavy streamlines along the jet centerline. When the vortices in the top and bottom shear layers are out of phase, as expected for the $m = \pm 1$ case, the upward and downward induced velocities are in the same cross-stream direction at the same streamwise location, as shown in Fig. 13b. As a result, the jet appears to be flapping by the induced velocity. In addition to the undulating motion of the jet column, the entrainment of the ambient air and the ejection of jet fluid into the ambient by the induced cross-stream velocity increases the lateral spread of the jet.

When the St_{DF} is increased to 0.72, the spacing of the adjacent vortices and the scale of the generated structures are significantly reduced (about halved), as shown in Fig. 13c. At this Strouhal number, the interaction between the vortices in the top and bottom shear layers is weaker due to the much smaller size of the generated vortices. Because of the smaller vortices and weaker interactions between the vortices and the jet column at this Strouhal number, the jet column did not significantly undulate. As shown in Figs. 6 and 7, the jet potential core was not significantly changed by the generated structures due to the limited interaction between top and bottom shear layers. As shown in Fig. 13d, the induced cross-stream velocity is confined to the thin top and bottom shear layers. Because the induced cross-stream velocity is reduced, it is expected that the entrainment and ejection of fluid would also be limited at this higher Strouhal number. As a result, the jet spreading was less enhanced than at $St_{DF} = 0.32$.

At higher St_{DF} of 1.08, the generated vortices are barely identifiable and are not organized, resembling those in the unforced jet. This is the reason that the mean flow (Figs. 6 and 7) and turbulence statistics (Fig. 11) for this forced case are similar to those for the baseline jet. For all other modes, the effects of St_{DF} on the spacing and size of the generated structures are very similar, and, therefore, the results are not presented here.

Figure 14 shows conditionally averaged streamwise and cross-stream velocity contours with superimposed Galilean streamlines for two additional modes, $m = 0$ and 1 at a St_{DF} of 0.32. As discussed

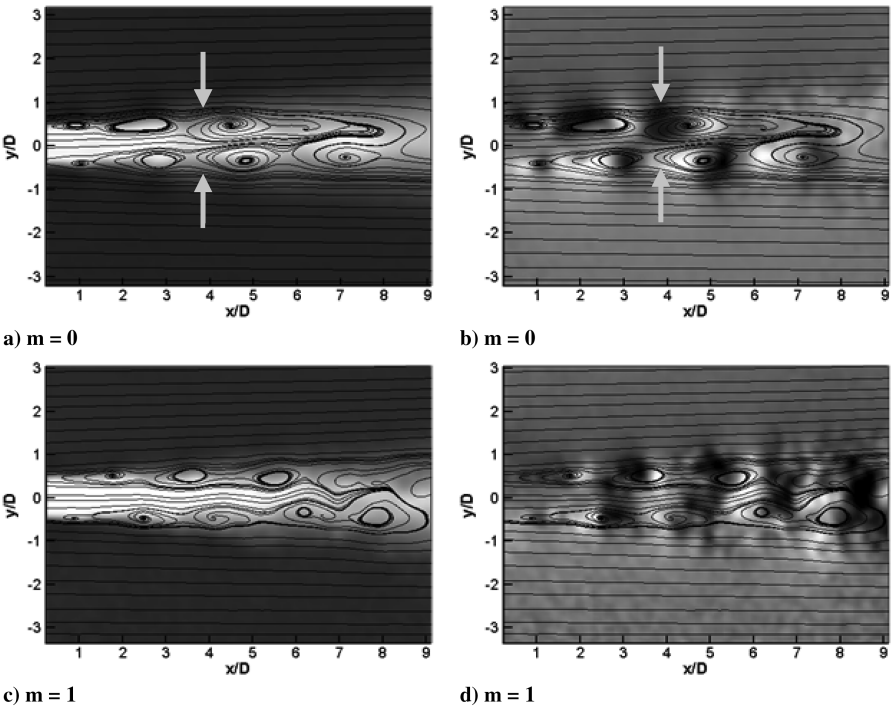

Fig. 14 Conditionally averaged Galilean streamlines and velocity magnitude contours for streamwise (left column) and cross-streamwise (right column) velocities for $m = 0$ and 1 modes at $St_{DF} = 0.32$.

earlier, the forcing at even- and odd-numbered azimuthal modes showed distinctly different turbulence characteristics, as shown in Fig. 12b, hence the selection of these two representative modes. For the axisymmetric mode ($m = 0$), the streamwise dimensions of the generated vortices are approximately the same as those for the flapping mode ($m = \pm 1$), but the cross-stream scales are smaller. Although the vortices at this mode appear to be as strong as those in the $m = \pm 1$ mode, the jet spreading is not as significant as seen in the $m = \pm 1$ case. The symmetry of the vortices seems to be responsible for the slower jet spreading. Because the generated structures for $m = 0$ are doughnut-shaped vortex rings, their development in the cross-stream direction is limited by this symmetry. When one part of the vortex ring attempts to grow toward the jet centerline, the opposite part also takes the same action, and thus the growth of the ring toward the jet centerline is limited due to the axisymmetric nature of the ring vortex. For the flapping mode ($m = \pm 1$), the vortex could grow toward the jet centerline easily by pushing the jet column to the other side, as shown in Fig. 13a. This limited growth of the vortex is partially responsible for the slower jet spreading as seen in Figs. 3 and 9.

In addition to the slower spreading for the $m = 0$ case, the jet centerline Mach number also decays relatively slowly, as seen in Fig. 9. It is conjectured that the jet centerline Mach number decay is closely related to the interaction between vortices and the jet column, which affects the entrainment of slow-moving fluid into the jet plume. The vortices at this mode do not cross the jet centerline because of their symmetry, as discussed earlier. As a result, the interaction is not as destructive as in the asymmetric cases (odd-numbered modes). The entrained fluid, from the much slower moving surrounding air near the trailing region of a ring (as indicated by arrows), goes through acceleration at the center of the ring due to self-induction. The self-induction seems to make the flow near the centerline accelerated, which counters the slowing action of the entrained fluid. Thus, the acceleration due to self-induction at the jet centerline and the symmetry of the vortex ring may be partially responsible for the slower centerline decay when compared with the other modes, as shown in Fig. 9.

Another interesting finding at $m = 0$ is that the jet centerline velocity seems to be going through a periodic change with the downstream location. The jet fluid at the center of a vortex ring is accelerated by self-induction of the vortex ring. In the trailing region of a vortex ring, the velocity is expected to decrease due to the entrainment of the slower moving ambient air, as indicated by the arrows in Fig. 14a. The entrainment by the induced velocity can be deduced from the cross-stream velocity contours, which show vertically induced velocity with opposite sign, as shown in Fig. 14b. Thus, two opposite actions of deceleration and acceleration take place around a vortex ring. These combined effects are most likely responsible for the periodic changing of the centerline velocity.

As discussed earlier, the development of TKE along the jet centerline for the $m = 0$ case was monotonic (Fig. 12a). The amplification of the centerline TKE is governed by the interaction between the vortices and the jet column. For odd-numbered modes, the flapping action of the jet plume across the jet centerline would increase the turbulence level. For the $m = 0$ case, the vortex rings grew monotonically and their identities were preserved for long downstream distances. This seems to be the cause for the monotonic development of TKE for $m = 0$.

For the $m = 1$ case, the vortical structures are smaller and weaker than those for $m = 0$ or $m = \pm 1$. The vortex generated at this mode is helical, and thus the coherence level in the cross-stream direction is smaller than $m = 0$ or $m = \pm 1$, where the generated vortices are vortical rings or spanwise structures, respectively. The jet column undulation and the induced velocity around a vortex are similar to those for the $m = \pm 1$ mode, as can be seen in Figs. 13 and 14. Thus, it is expected that the vortex dynamics at this mode will be similar to those at $m = \pm 1$ because the vortex patterns are very similar. However, the interaction between vortices across the jet column and cross-stream velocity induced by self-induction are expected to be slightly weaker than those at $m = \pm 1$. This reduced interaction and induced velocity may be responsible for the reduced jet spreading, as shown in Fig. 9c.

The development of anisotropy was discussed earlier (Fig. 12b) and showed the streamwise velocity fluctuations to be largest for the axisymmetric modes (even-numbered modes). As can be inferred from Fig. 14, the cross-stream velocity fluctuations are suppressed because of the symmetric nature of the vortices across the jet centerline, as shown in Fig. 14b. The induced velocity on the upstream side of a pair of vortices on the top and bottom shear layers is downward and upward, respectively, as indicated by arrows in Fig. 14b. Also, the streamwise velocity fluctuation is more likely amplified due to self- or mutual-induction. This explains why the

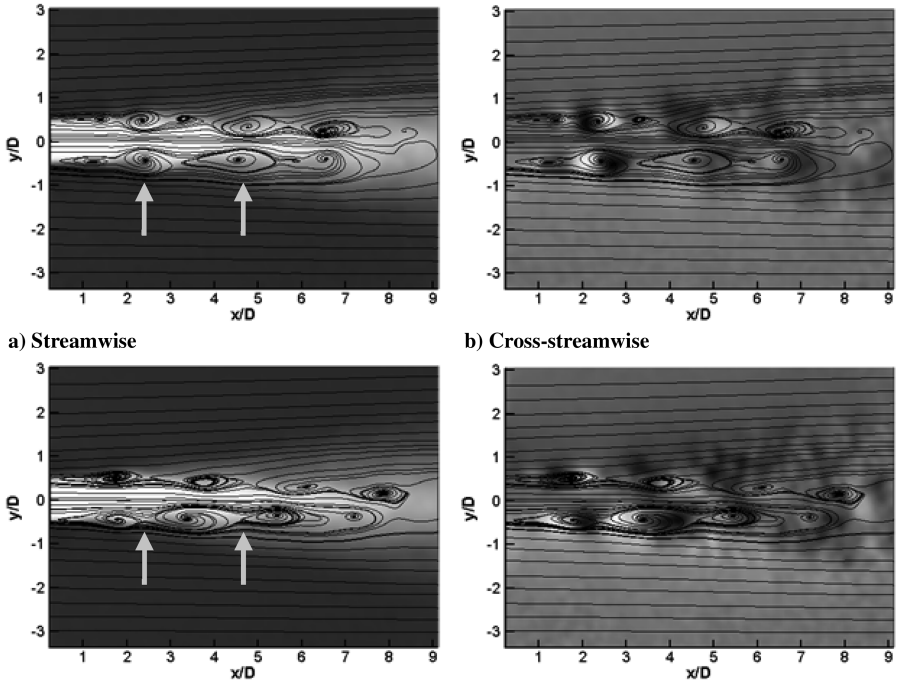

a) Streamwise

b) Cross-streamwise

c) Streamwise, 180° out of phase with the image in a

d) Cross-streamwise, 180° out of phase with the image in b

Fig. 15 Conditionally averaged Galilean-decomposed velocity components with superimposed streamlines for $m = \pm 2$.

anisotropy is decreased for the even-numbered modes. On the other hand, the induced cross-stream velocity fluctuations are in the same direction at a given x/D for the odd-numbered modes, as observed in Fig. 14d. This leads to more amplification in the cross-stream velocity fluctuations, and is responsible for the increased anisotropy for the odd-numbered modes. The level of interaction across the jet centerline can be higher earlier for the even-numbered modes than for the odd-numbered ones, as can be observed in Figs. 14a and 14d. This is associated with the earlier or later saturation of anisotropy for the even- or odd-numbered modes, respectively.

As mentioned in Sec. III.B, the centerline Mach number distribution for $m = \pm 2$ is comparable to that of $m = \pm 1$, although the jet spreading is not. The vortex dynamics can offer some clues for this difference. Conditionally averaged, Galilean-decomposed velocity components with superimposed streamlines are shown in Fig. 15 for two phases. The bottom images are 180 deg out of phase relative to the top ones. The arrows in Fig. 15a indicate the center of two adjacent vortices. However, the arrows at the same x/D location in Fig. 15c point to a location between two consecutive vortices, because the two images are out of phase. Although the vortex pattern is similar to that of the $m = 0$ mode, the vortices at this mode are expected to be quasi-two-dimensional, because the actuators on the vertical and horizontal planes are operated out of phase. This will be further discussed later using cross-stream velocity fields.

The following discussion is based on the assumption that the generated vortices are spanwise or at least quasi spanwise. This is confirmed by taking images in the visualized cross section (not published) of an ideally expanded Mach 1.3 jet at $x/D = 4$. The high-speed jet column is squeezed in the vertical direction between a pair of horizontally aligned vortices at the location indicated by the two arrows in Fig. 15a. The corresponding jet cross section is shown schematically in Fig. 16a. In a half-cycle of the forcing period, a vertically oriented pair of vortices pass through the same downstream location (indicated by the arrows in Fig. 15c) and cause the high-speed plume to be squeezed vertically, as shown schematically in Fig. 16b. This alternating squeezing action by vertically and horizontally aligned pairs of vortices is probably responsible for the relatively fast decay of the jet centerline Mach number. On the other hand, it is expected that the mixing/spreading performance of pairs of vortices at this mode would not be large, as

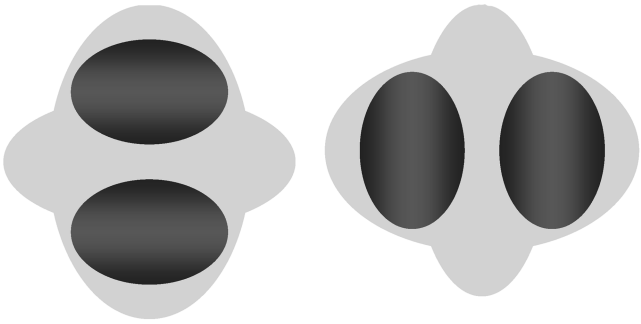

a) At an x/D location indicated by an arrow in Fig. 15a

b) At an x/D location indicated by an arrow in Fig. 15c

Fig. 16 Schematic of the jet cross section for $m = \pm 2$. The light gray tone represents the jet cross section and the darker ellipses indicate large-scale structures.

the vortices are symmetric across the jet centerline as explained for the $m = 0$ case.

E. Convection Velocity of Large-Scale Structures

The convection velocity of the generated structures due to forcing was calculated by the same method discussed earlier. A correlation window in an instantaneous velocity field was selected, covering approximately 75% of the streamwise spacing of two adjacent large-scale structures and the entire width of the shear layer. As in Samimy et al. [10], one can get the spatial-correlation profiles along any streamwise line, for example, the jet lip line, from such two-dimensional spatial correlations. The spatial-correlation profiles for several Strouhal numbers are shown in Fig. 17 for $m = \pm 1$. When there are periodic structures in the shear layer, the spatial correlation is similar to an amplitude-modulated sinusoidal wave. For the baseline jet, there is no periodic motion. When the jet is forced, large-scale periodic structures are generated, as indicated by the multiple local peaks of the amplitude-modulated sinusoidal wave. As discussed earlier, the peak-to-peak distance is the wavelength (spacing) of the generated structures. The convection velocity is

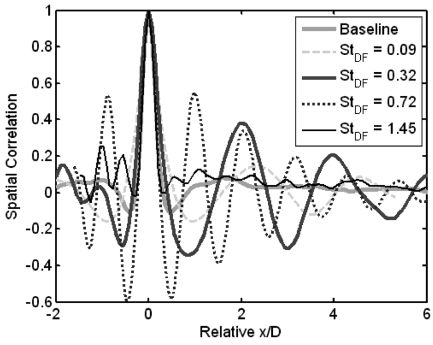

Fig. 17 Spatial correlation along the lip line of the jet for several Strouhal numbers at $m = \pm 1$ mode.

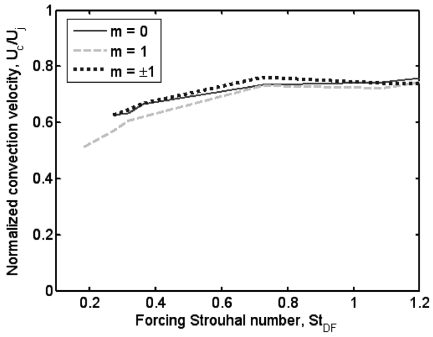

Fig. 18 Convection velocity for three modes.

obtained by multiplying the calculated wavelength by the forcing frequency. The calculated convection velocity for the three forcing modes of $m = 0$, 1, and ± 1 are shown in Fig. 18.

As the St_{DF} is increased, the normalized convection velocity is increased for all three modes. At the lowest forcing Strouhal number, the convection velocity is close to the theoretically predicted value of 0.52. It seems that the normalized convection velocity converges to about 0.77 at St_{DF} numbers greater than about 0.72. The present normalized convection velocity, calculated from instantaneous velocity fields, is slightly larger than that obtained from qualitative flow visualization results in a Mach 1.3 jet for St_{DF} numbers of 0.3–0.65 [10]. Their results showed a constant value of 0.67 over this Strouhal number range. The convection velocity measured in a supersonic round jet at Mach numbers from 1.6 to 1.86 was from 0.7 to 0.78 [22], which agrees well with the present results at higher Strouhal number forcing cases. Petitjean et al. [22] used a two-point space-time correlation-based technique to calculate convection velocity in the cold jet. Bridges [23] also measured convection velocity in cold and heated circular jets by using a dual-PIV system. The normalized convection velocity in his case is 0.75 at an acoustic Mach number of 0.9 in a cold jet. His results also compare well with the present results at higher St_{DF} numbers. In a forced jet by glow discharge, the normalized convection velocity measured by Troutt and McLaughlin [21] is about 0.8 for a St_{DF} of 0.3–0.8 in a Mach 2.1 jet. Although their results compare well with the present values at higher Strouhal numbers, they did not see an increase in convection velocity as the St_{DF} was increased from 0.3 to 0.8, which potentially could indicate a lack of actuator authority to force the jet column instability.

IV. Conclusions

A Mach 0.9 circular jet with a Reynolds number based on the nozzle exit diameter of 7.6×10^5 was controlled by using eight localized arc filament plasma actuators, equally distributed azimuthally just upstream of the nozzle exit. Two-component PIV measurements were obtained on a streamwise plane passing through the jet centerline. The average streamwise velocity contours, turbulence statistics, centerline Mach number distribution, and jet width development were used to investigate the effects of St_{DF} and forcing azimuthal mode. The forcing Strouhal number was varied from 0.09 to 3.08, and the azimuthal modes explored included $m = 0$–3, ± 1, ± 2, and ± 4, which are the only available modes when using eight actuators. For all azimuthal modes explored here, the most effective forcing was around a Strouhal number of 0.3, which is in agreement with the results in the literature, except for mode $m = 3$, which showed the best spreading at a forcing Strouhal number of 0.09. The flapping mode ($m = \pm 1$) resulted in the best entrainment and mixing or jet spreading rate.

The two-dimensional turbulence kinetic energy was also significantly increased by forcing at low Strouhal numbers. At high St_{DF} numbers, the turbulence level was reduced for some azimuthal modes, but remained about the same for the rest. For even-numbered azimuthal modes, the cross-stream velocity fluctuations were suppressed along the jet centerline by the symmetry of the vortices, but turbulence levels in the streamwise direction were amplified, resulting in decreased anisotropy. On the other hand, the cross-stream component of TKE was more amplified for odd-numbered azimuthal modes due to the undulating jet column. As a result, the anisotropy was increased. Because the maximum interaction between the top and bottom vortices occurred earlier for the even-numbered modes, the anisotropy saturated earlier than that for the odd-numbered modes.

Conditionally averaged velocity fields and convection velocity of large-scale structures were obtained by using two-dimensional planar spatial correlation. From conditionally averaged velocity fields and convection velocity, Galilean streamlines were obtained that revealed the nature of the generated large-scale structures and their role in the jet development. The nature of jet spreading and development was explained by the dynamics of large-scale structures, including mutually and/or self-induced velocity fields. The difference in turbulence statistics development was also explained by the vortex dynamics. The results showed that the spacing of the generated vortices depends strongly on the St_{DF}. However, the dimension and pattern of the vortices depend not only on the forcing frequency but also on the forcing azimuthal modes. The measured convection velocity, especially at higher St_{DF} numbers, compared well with results in the literature.

Acknowledgments

This research is supported by a NASA grant (NNX07AC86A). The support and fruitful discussions with Ohio State University colleagues Igor Adamovich and Munetake Nishihara, and NASA colleagues James Bridges and Cliff Brown, are greatly appreciated.

References

[1] Zaman, K. B. M. Q., and Hussain, A. K. M. F., "Turbulence Suppression in Free Shear Flows by Controlled Excitation," *Journal of Fluid Mechanics*, Vol. 103, 1981, pp. 133–159. doi:10.1017/S0022112081001274

[2] Freymuth, P., "On Transition in a Separated Laminar Boundary Layer," *Journal of Fluid Mechanics*, Vol. 25, 1966, pp. 683–704. doi:10.1017/S002211206600034X

[3] Michalke, A., "On Spatially Growing Disturbances in an Inviscid Shear Layer," *Journal of Fluid Mechanics*, Vol. 23, 1965, pp. 521–544. doi:10.1017/S0022112065001520

[4] Cho, S. K., Yoo, J. Y., and Choi, H., "Vortex Pairing in an Axisymmetric Jet Using Two-Frequency Acoustic Forcing at Low to Moderate Strouhal Numbers," *Experiments in Fluids*, Vol. 25, No. 4, 1998, pp. 305–315. doi:10.1007/s003480050234

[5] Crow, S. C., and Champagne, F. H., "Orderly Structure in Jet Turbulences," *Journal of Fluid Mechanics*, Vol. 48, 1971, pp. 547–591. doi:10.1017/S0022112071001745

[6] Gutmark, E., and Ho, C. M., "Preferred Modes and the Spreading Rated of Jets," *Physics of Fluids*, Vol. 26, No. 10, 1983, pp. 2932–2938. doi:10.1063/1.864058

[7] Ho, C.-M., and Huerre, P., "Perturbed Free Shear Layers," *Annual Review of Fluid Mechanics*, Vol. 16, Jan. 1984, pp. 365–424. doi:10.1146/annurev.fl.16.010184.002053

[8] Samimy, M., Adamovich, I., Webb, B., Kastner, J., Hileman, J., Keshav, S., and Palm, P., "Development and Characterization of

Plasma Actuators for High Speed and Reynolds Number Jet Control," *Experiments in Fluids*, Vol. 37, No. 4, 2004, pp. 577–588. doi:10.1007/s00348-004-0854-7

[9] Samimy, M. J., Kim, J.-H., Kastner, J., Adamovich, I., and Utkin, Y., "Active Control of a Mach 0.9 Jet for Noise Mitigation Using Plasma Actuators," *AIAA Journal*, Vol. 45, No. 4, 2007, pp. 890–901. doi:10.2514/1.27499

[10] Samimy, M., Kim, J.-H., Kastner, J., Adamovich, I., and Utkin, Y., "Active Control of High Speed and High Reynolds Number Jets Using Plasma Actuators," *Journal of Fluid Mechanics*, Vol. 578, May 2007, pp. 305–330. doi:10.1017/S0022112007004867

[11] Utkin, Y., Keshav, S., Kim, J.-H., Kastner, J., Adamovich, I., and Samimy, M., "Use of Localized Arc Filament Plasma Actuators for High Speed Jet Control," *Journal of Physics D: Applied Physics*, Vol. 40, Feb. 2007, pp. 685–694. doi:10.1088/0022-3727/40/3/S06

[12] Samimy, M., Kastner, J., Kim, J.-H., Utkin, Y., Adamovich, I., Bridges, J., and Brown, C., "Flow and Noise Control in High Speed and High Reynolds Number Jets Using Plasma Actuators," AIAA Paper 2006-2846, 2006.

[13] Kastner, J., Hileman, J., and Samimy, M., "Exploring High-Speed Axisymmetric Jet Noise Control Using Hartmann Tube Fluidic Actuators," AIAA Paper 2004-0186, 2004.

[14] Melling, A., "Tracer Particles and Seeding or Particle Image Velocimetry," *Measurement Science and Technology*, Vol. 8, No. 12, 1997, pp. 1406–1416. doi:10.1088/0957-0233/8/12/005

[15] Bridges, J., and Wernet, M. P., "Turbulence Measurements of Separated Flow Nozzles with Mixing Enhancement Features," AIAA Paper 2002-2484, 2002.

[16] Adrian, R., Christensen, K., and Liu, Z., "Analysis and Interpretation of Instantaneous Turbulent Velocity Fields," *Experiments in Fluids*, Vol. 29, No. 3, 2000, pp. 275–290. doi:10.1007/s003489900087

[17] Kline, S. J., and Robinson, S. K., "Quasi-Coherent Structures in the Turbulent Boundary Layer, I: Status Report on a Community-Wide Summary of the Data," *Near-Wall Turbulence: 1988 Zoran Zaric Memorial Conference*, edited by S. J. Kline, and N. H. Afgan, Hemisphere, New York, 1990, pp. 200–217.

[18] Robinson, S. K., Kline, S. J., and Spalart, P. R., "A Review of Quasi-Coherent Structures in a Numerically Simulated Turbulent Boundary Layer," NASA TM 102191, 1989.

[19] Konstantinidis, E., Balabani, S., and Yianneskis, M., "Conditional Averaging of PIV Plane Wake Data Using a Cross-Correlation Approach," *Experiments in Fluids*, Vol. 39, No. 1, 2005, pp. 38–47. doi:10.1007/s00348-005-0963-y

[20] Kastner, J., Kim, J.-H., and Samimy, M., "Toward Better Understanding of Far-Field Radiated Noise Mechanisms in a High Reynolds Number Mach 0.9 Axisymmetric Jet," AIAA Paper 2008-0007, Jan. 2008.

[21] Troutt, T. R., and McLaughlin, D. K., "Experiments on the Flow and Acoustic Properties of a Moderate-Reynolds Number Supersonic Jet," *Journal of Fluid Mechanics*, Vol. 116, 1982, pp. 123–156. doi:10.1017/S0022112082000408

[22] Petitjean, B. P., McLaughlin, D. K., and Morris, P. J., "An Experimental Investigation of Density Gradient Fluctuations in High-Speed Jets Using Optical Deflectometry," AIAA Paper 2006-2533, 2006.

[23] Bridges, J., "Effect of Heat on Space-Time Correlations in Jets," AIAA Paper 2006-2534, 2006.

N. Chokani
Associate Editor